Defects in vibrated monolayers of equilateral triangular prisms

Jorge Vega
Departamento de Física Teórica de la Materia Condensada, Universidad Autónoma de Madrid, E-28049 Madrid, Spain

Enrique Velasco*
Departamento de Física Teórica de la Materia Condensada, Instituto de la Materia Condensada (IFIMAC) and Instituto de Ciencia de Materiales Nicolás Cabrera, Universidad Autónoma de Madrid, E-28049 Madrid, Spain

Yuri Martínez-Ratón†
Universidad Carlos III de Madrid, Departamento de Matemáticas, Grupo Interdisciplinar de Sistemas Complejos (GISC), 28911 Leganés, Spain

(Received 9 May 2025; accepted 11 November 2025; published 2 December 2025)

We present experimental results in which a quasimonolayer of grains, shaped as equilateral triangular prisms, is vertically vibrated within circular and square confining cavities. The system exhibits a fluid phase characterized by sixfold orientational order. However, the specific geometries of the cavities frustrate this order, leading to the excitation of topological defects that adhere to topological principles. We analyze the distribution of topological charges of these defects and their evolution as a function of the container geometry. In particular, we find that in the circular cavity, both the number and charge of defects remain constant in the steady-state regime, with only defects of charge $+1$ being excited. In contrast, within the square cavity—with the same topology as the circular cavity—some defects become pinned to the corners of the cavity, developing charges of $+1$ or $+2$. Additionally, free defects with charges of ± 1 can be excited. Notably, dynamic events occur, such as the fusion of two defects or the creation of two defects from a single one. These events are governed by the conservation of total charge within the cavity and give rise to various system configurations, with rapid transitions between them. The observed dynamic fluctuations in topological charge are remarkable, influenced by both particle shape and cavity geometry. This system of vertically vibrated (dissipative) granular monolayers presents a unique and simple platform for studying topological phenomena, with potential implications for topological effects in equilibrium-oriented fluids.

DOI: 10.1103/nzy9-2c7d

I. INTRODUCTION

Vertically vibrated monolayers of granular particles played an important role in the understanding of crystallization [1–5]. However, recently the tendency of anisotropic grains to form liquid-crystalline phases has been emphasized [6]. These dissipative monolayers behave in some respects as their thermal-equilibrium counterparts [6–13]. The liquid-crystalline phase diagram of quasimonolayers of cylinders (projecting as hard rectangles on the plane) has been mapped out as a function of density and particle aspect ratio [11]. The diagram shows many similarities with that of equilibrium hard rectangular particles [14].

Liquid-crystalline defects have been studied for a long time and continue to arise great interest [15,16]. Recently, the area of active nematics has expanded this interest even further, with nonequilibrium phenomena that allow defect dynamics to be studied *in situ* [17–20]. Defects in two dimensions have been shown to drive the self-assembly of colloidal particles [21]. Also, the presence of patchy colloids in a nematic fluid generates interesting defect topologies near their surfaces [22,23].

Defects have also been observed in granular two-dimensional (2D) matter [12]. Experiments on hard rectangles have shown the excitation of defects in a circular cavity, with their number and topological charge exactly as predicted by topology [24]. The four defects behave as repulsive particles with interactions mediated by the orientational stiffness of the fourfold symetric, 4-atic liquid-crystal phase. The structure of the nematic field in the neighborhood of the defects indicates that they have a topological charge $+1$, giving a total charge of $+4$ within the cavity, as predicted by topology [25,26]. Recent experimental and theoretical studies on colloidal monolayers of hard discorectangles in annular confinement have also shown the formation of smectic textures with different competing defect structures [27].

Recent theoretical investigations, based on Landau-de Gennes theory, density functional theory, and Monte Carlo (MC) simulations, have examined the influence of geometrical confinement, particularly corners in cavities and protruding

*Contact author: enrique.velasco@uam.es
†Contact author: yuri@math.uc3m.es

Published by the American Physical Society under the terms of the Creative Commons Attribution 4.0 International license. Further distribution of this work must maintain attribution to the author(s) and the published article's title, journal citation, and DOI.

obstacles, on the formation and stability of topological defects in systems of rodlike particles [28–30]. In the bulk, such systems exhibit 2-atic (uniaxial nematic) order, which supports defects with winding numbers of $k = \pm 1/2$.

It is interesting to explore whether these findings, pertaining to systems exhibiting 2-atic or 4-atic symmetries, can be extended to other particle shapes, whose intrinsic ordering gives rise to higher-order symmetries in the fluidized granular monolayer. In such cases, confinement within cavities of varying geometries may similarly determine the number and charge of the topological defects through symmetry-based topological arguments.

The present work considers a system composed of hard equilateral triangles, which forms a 6-atic phase in bulk [31–33]. Accordingly, the relevant topological defects in this system are characterized by winding numbers of $\pm 1/6$, which reflect the sixfold rotational symmetry of the underlying order. While previous studies typically quantify defect topology using the winding number k, and apply conservation laws by summing over all winding numbers in the cavity, resulting from the presence of confining corners or obstacles, we adopt a complementary formulation. Specifically, we use the topological charge of a defect, $q = pk$, where p denotes the symmetry order of the p-atic phase ($p = 6$ in our case). This approach provides a direct link between defect topology and the underlying symmetry of the ordered phase. The two frameworks, one based on winding numbers and the other on topological charges, are mathematically equivalent in terms of the conservation laws that arise from the topological constraints imposed by corners and obstacles.

In this paper, we explore the behavior of grains with the shape of an equilateral triangular prism, confined into cavities of different geometries. As mentioned before, these particles exhibit an oriented fluid phase with sixfold symmetry (6-atic phase) in equilibrium [31–33]. We show that granular monolayers made of these particles also show these symmetries. However, their behavior is greatly affected by the geometry of the container. We have explored two types of cavities: circular and square, both topologically equivalent. Circular and square cavities are both incompatible with the inherent symmetry of the 2D fluid, and consequently, defects are expected to be excited in the system, with a total topological charge given by the genus of the cavity, the total charge being equal to $+6$. We will see that this holds for equilateral triangles, where six defects with charge $+1$ are formed in the circular cavity. In contrast, the square cavity may generate from four to up to seven defects of different charges, while still maintaining the overall charge. The distribution and dynamics of the charges in this case are rather peculiar, with different configurations and number of defects dynamically changing in time.

Vertically vibrated granular monolayers are a convenient experimental system to explore the interplay between liquid-crystal symmetries and boundary geometry, which is governed by the rules of topology. Access to different types of defects and their dynamics can be easily tuned to create geometric frustration of various sorts. Equilibrium elastic theory and topological considerations for liquid-crystalline systems seem to explain the phenomenology of the granular monolayers, at least under reasonable assumptions. Also, the effect of dissipation and nonequilibrium phenomena can be assessed by conducting thermal-equilibrium simulations of similar systems in 2D; possibly different behaviors can be inferred from a comparison between the two systems.

The article is organized as follows. In Sec. II, we introduce the elastic theory for a two-dimensional liquid crystal and the structure of possible defects found in the system. These defects should abide by the rules of topology in systems with inherent orientational order. Section III presents the experimental setup and gives some details on the MC simulations and the protocols used to prepare the systems. Results are presented in Sec. IV, which also contains a detailed discussion of the findings. Section V presents some conclusions. Finally, in the Appendix, we generalize the topological rules governing the charge and number of defects arising from the confinement of triangular prisms within circular and square cavities to cavities of any regular polygonal shape.

II. ELASTIC THEORY AND TOPOLOGICAL DEFECTS

The concept of geometric frustration describes a situation where some kind of local order cannot propagate to the entire system. Geometric frustration can be caused by appropriate boundary conditions imposed to the system, as it occurs in our experiment. Indeed, the director field defined by the orientation of anisotropic particles in 2D is a perfect example of a system that can develop geometric frustration. In our particular case, the sixfold symmetry of the 6-atic phase is incompatible with both the circular and the square symmetry of the boundary. The 6-atic symmetry can be expressed locally by the invariance of the angular distribution function $f(\phi)$ with respect to rotations of $\pi/3$, i.e., $f(\phi) = f(\phi + \pi/3)$, $f(\phi)$ being the angular probability density of a particle axis forming an angle ϕ with respect to the local nematic director. In the present case, the particle axis of equilateral triangles (the cross sections of the triangular prisms) points from the barycenter to one of its vertices. Obviously, there are three equivalent axes.

In order to understand how such a system can manifest geometric frustration due to the boundary conditions, we need to invoke some topology concepts based on the Euler theorem of topology [26]. Briefly, this theorem relates the number of vertices V, edges E, and faces F of a tessellation of an orientable closed 2D surface as follows:

$$V - E + F = \chi = 2(1 - g) - h, \tag{1}$$

where χ is the Euler characteristic of the surface, which can be expressed in terms of two integers, g the genus (representing the number of "handles" of the surface) and h (the number of boundaries or "holes" of the surface). The theorem can be rephrased [26] to show that the total topological charge q_t of a system satisfies the following equation:

$$q_t = \sum_{i=1}^{N} q_i = p\chi, \tag{2}$$

where $\{q_i\}$ are the individual topological charges of the defects and p is the symmetry of the director field (the local orientation is defined modulo $2\pi/p$). The ratio between the charge of a defect q and the symmetry of the field p is called the winding number of the defect $k = q/p$. For example, a simple

vector field ($p = 1$) in a sphere (no handles or holes, so $\chi = 2$) can have two topological defects with charge $q = 1$, that is, one source and one sink, a case corresponding to the famous "hairy ball" theorem [34]. In our case, the director field of the 6-atic phase has sixfold symmetry ($p = 6$) and both the circular and square cavities are topologically equivalent to a disk (without handles but with one boundary, giving $\chi = 1$), and therefore $q_t = +6$. Note that Euler's theorem only determines the total topological charge in the system, not the number of defects or their individual charges.

The nematic director field in the neighborhood of a single defect is different according to the topological charge of the defect. In this work, we use the director field in our granular samples to identify the value of the charges. The relation between charge and director field is obtained from Frank's elastic theory [35], which expresses the cost in free energy associated with a spatial deformation of the local nematic director $\boldsymbol{n}(\boldsymbol{r})$ as

$$\mathcal{F}_{\rm el}[\boldsymbol{n}] = \frac{1}{2}\int_A d\boldsymbol{r}[K_1(\mathrm{div}\,\boldsymbol{n})^2 + K_3|\boldsymbol{n}\times \mathrm{rot}\,\boldsymbol{n}|^2], \tag{3}$$

with K_1 and K_3 the elastic constants for splay and bend deformations, respectively. Considering 2D nematics, we can write $\boldsymbol{n} = (\cos\theta, \sin\theta)$, with θ the angle of the nematic director with respect to a fixed laboratory frame. Assuming the one-constant approximation ($K_1 = K_3 \equiv K$, which is exact only for 4-atic ordering), the elastic free energy for a 2D p-atic phase is

$$\mathcal{F}_{\rm el}[\theta] = \frac{K}{2}\int_A d\boldsymbol{r}|\nabla\theta|^2. \tag{4}$$

Functional minimization with respect to θ provides the Euler-Lagrange equation $\nabla^2\theta = 0$, which generates harmonic solutions. Assuming a defect of winding number k at the origin, which represents a point charge, the constraint $\int_\gamma d\theta = 2\pi k$ must be satisfied (meaning that the closed line integral along a circle of unit radius γ, surrounding the defect, is equal to $2\pi k$). Solutions of the equation satisfying the constraint are given by $\theta = k\varphi + \theta_0$, where φ is the angle in polar coordinates and θ_0 is a phase. The equilibrium free energy is then

$$\mathcal{F}_{\rm el} = \pi K k^2 \ln\left(\frac{R}{a}\right), \tag{5}$$

with a the radius of the core of the defect and R the system length. In case of having N defects of the same core size a, the associated elastic free energy can be evaluated similarly [36] to give

$$\frac{\mathcal{F}_{\rm el}}{\pi K} = \left[\left(\sum_{i=1}^{N} k_i\right)^2 \ln\left(\frac{R}{a}\right) + 2\sum_i\sum_{j>i} k_i k_j \ln\left(\frac{a}{r_{ij}}\right)\right], \tag{6}$$

with r_{ij} the relative distance between the ith and jth defects. From this, we can see that the free energy of two interacting defects with opposite charges ($k_1 + k_2 = 0$) does not depend on the system size R, so the logarithmic divergence when $R \to \infty$ disappears. Also, it is obvious that the interaction energy from the second term is a decreasing (increasing) function of r_{12} when $k_1k_2 > 0$ ($k_1k_2 < 0$) implying that topological charges of same signs repel (attract) each other. Also, the conservation of the total topological charge, equal to $q_t + 6$, is equivalent to the constraint $\sum_{i=1}^{N} k_i = 1$; i.e., the total winding number of the defects is equal to 1. Consequently, the second term in Eq. (6) is the only one responsible for the difference between the elastic free energies of different defect configurations.

As mentioned before, the director field will be used to identify the charge of individual defects. In the following, we calculate such a field for the different lowest-order defects expected in our system. Given the field $\theta(\boldsymbol{r}) = \theta(x, y) = \theta(\varphi)$, the curves whose tangent lines have slopes $dy/dx = \tan\theta$ correspond to the one-parametric family of curves resulting from the solution of the first-order equation

$$\frac{dy}{dx} = \frac{r'\sin\varphi + r\cos\varphi}{r'\cos\varphi - r\sin\varphi} = \tan\theta = \tan(k\varphi + \theta_0), \tag{7}$$

where $r' = dr/d\varphi$. Solving for r',

$$r' = r\cot[(k-1)\varphi + \theta_0]. \tag{8}$$

After integration, we arrive at

$$r(\varphi) = r_0|\sin[(k-1)\varphi + \theta_0]|^{1/(k-1)}. \tag{9}$$

The 6-atic field around defects with $k = \pm 1/6$ (selecting phases $\theta_0 = 0,\ \pm\pi/3$), i.e., with topological charges $q = \pm 1$, is shown in Figs. 1(a) and 1(b). We note the characteristic pentagonal ($q = +1$) or heptagonal ($q = -1$) patterns about the defect, either convex ($q = +1$) or nonconvex ($q = -1$), depending on the sign of the charge.

Note that these director configurations refer to free topological defects. As we will promptly see, defects in the circular cavity are close to the cavity wall, but they can still be considered as free defects. In contrast, in the square cavity there are always defects that are pinned to the corners of the square cavity; in this case, it is necessary to redefine what we mean by winding number and topological charge. Because it is reasonable to expect that anchoring conditions at the walls are strong, a set of triangles will always orient with one of their three equivalent sides parallel to the walls, while their nearest neighbors (the complementary set) have one of their vertexes in contact with the wall and their heights perpendicular to it, in such a way that the two sets of particles form a perfect monolayer. As a consequence, the director field is forced to be aligned perpendicular to the walls, and therefore rotates by 90° at the corner. To this, we must add the rotation of the field from one wall to the other around the defect following a contour inside the cavity, which accumulates an angle of ±30°; see Figs. 2(a) and 2(b). The final result is that the defected structures at the corners can be interpreted as having charges of $q = +1$ and $q = +2$. In fact, this result is equivalent to calculating the configuration of the director field around a free defect with an effective winding number of $\tilde{k} = \pm 1/3$, extracting the field structure from the specific quadrant shown in Figs. 2(a) and 2(b), and adding the constant wall rotation angle of 90°. The total rotation of the pinned defect is 90° ± 30°, giving angles of 60° ($q = +1$) and 120° ($q = +2$), and consequently, the winding numbers of pinned defects are $k = \frac{\pi/3}{2\pi} = \frac{1}{6}$ ($q = +1$) and $k = \frac{2\pi/3}{2\pi} = \frac{1}{3}$ ($q = +2$).

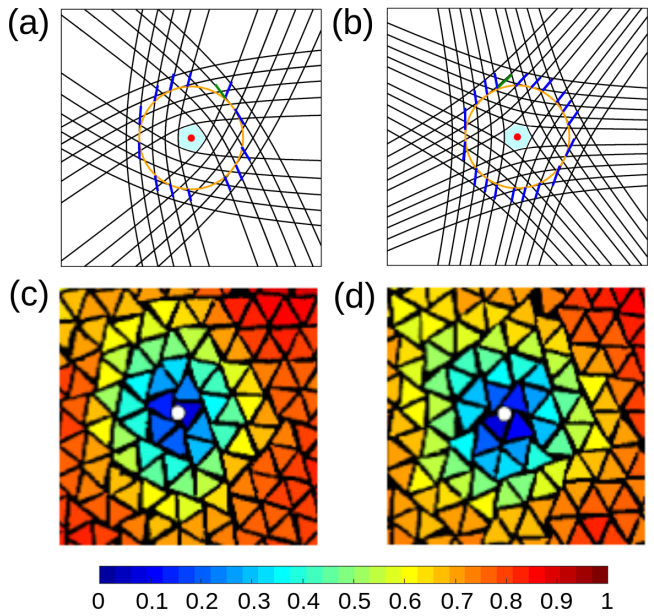


FIG. 1. (a) Director field in the neighborhood of free defects (filled circle) of the 6-atic orientational field corresponding to a topological charge of $+1$. (b) Same as panel (a), but for a charge of -1. Blue segments in both panels indicate the rotation of the director along the circumference shown. The total rotation angles are $\pi/3$ for panel (a) and $-\pi/3$ for panel (b). Defect core geometries are shaded. (c) Particle configurations of the granular monolayer in a region identified as a defect of charge $+1$. Colors indicate the value of Q_6. (d) Same as panel (c), but for a defect of charge -1. Note the close similarities between the structures in panels (a) and (c) and in panels (b) and (d).

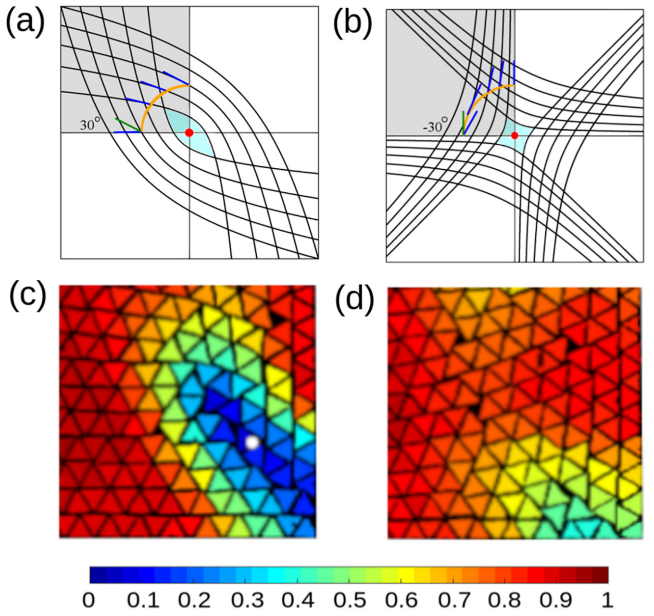


FIG. 2. Director fields in the neighborhood of pinned defects (filled circle) of charge (a) $q = +2$ and (b) $q = +1$. Relevant structures of the fields are those inside the shaded quadrants. The total topological charge in each case can be calculated as $q = (\theta + \pi/2)/(2\pi/p)$, with $\theta = \pi/6$ for the $q = +2$ charge and $\theta = -\pi/6$ for the $q = +1$ charge, with $p = 6$ as corresponds to a 6-atic symmetry. Rotation angles $\theta = \pm\pi/6$ can be obtained by imposing free defect structures with a global rotation angle of $\pm 2\pi/3$ (i.e., with effective winding numbers $\tilde{k} = \pm 1/3$). (c) Particle configurations of the granular monolayer in a corner region identified as a defect of charge $+2$. Colors indicate the value of Q_6. (d) Same as panel (c), but for a defect of charge $+1$. Note the close similarities between the structures in panels (a) and (c) and in panels (b) and (d).

Free defects of charge $q = +2$ are not expected to get stabilized in a 2D nematic due to their large elastic energy, but can be partially screened when anchored to the corner of a square and, as seen in Sec. IV, help explain the global topological behavior of the granular fluid in the square cavity.

In the Appendix, we generalize these topological rules to determine the charges of pinned defects and the number of possible defect configurations, including free ones, for any confining cavity shaped as a regular polygon with n sides.

III. EXPERIMENTAL SETUP AND MONTE CARLO SIMULATION

The experimental setup is similar to that used in previous work by our group [12,13,24], and has been described elsewhere. In brief, particles made of nonmagnetic steel with the shape of an equilateral triangular prism are confined into a horizontal cavity (Fig. 3), forming a quasimonolayer. A transparent upper lid made of methacrylate confines the particles vertically into a space with a height l, with $w < l < 2w$. $w = 1$ mm is the thickness of the triangular prisms. This allows particles to move vertically, while preventing two particles to stack one on top of the other. Their lateral size is $s = 4$ mm, and l must be smaller than the height of the particles, $s\sqrt{3}/2$, so that a particle cannot stand up on one of its edges. The cavities, either circular or square, have a size $L = 15$ cm across, and are vibrated vertically with frequency $\nu = 100$ Hz, at an effective gravity $\Gamma = A\nu^2/g = 2 - 3$ (with A the amplitude and g the gravity constant), such that the monolayer exhibits uniform density throughout the cavity. Particle configurations are recorded from above using a charged-coupled device camera at a rate of 4 pictures/min.

Experiments typically run for 2–3 h, and the system needs less than 1 h to reach the steady state. Particles are identified using our own code, which also extracts their position and orientation. The latter cannot be correctly identified with the standard procedure of using the ellipse that best fits the set of pixels pertaining to the particle edges: A circle will always give the best fit for equilateral triangles, and consequently, no particle orientation can be extracted from our algorithm. To solve this problem, a function was programmed that produced particle orientations as follows. The distance from the particle's barycenter to its edge, as a function of the angular variable in polar coordinates, can be calculated analytically for any given particle orientation angle (measured with respect to a fixed coordinate frame). Alternatively, this distance can be computed from the set of pixels defining the particle edges, using an edge-detection algorithm. By minimizing the sum of the squared differences between the analytical and experimental distances with respect to the particle orientation angle, an approximate value for the orientation angle can be obtained. This procedure yields highly accurate results for the particle's

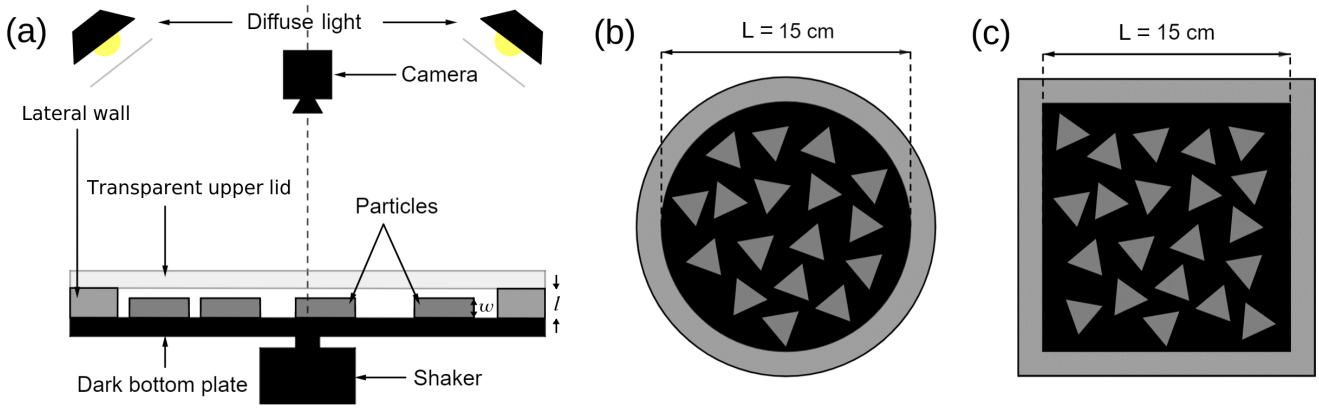


FIG. 3. (a) Schematic of the experimental setup (lateral view). (b) Zenithal view of the circular cavity. (c) Zenithal view of the square cavity.

orientational field. Using these orientations, the set of order parameters are calculated (see Sec. IV), and color maps for the order parameters Q_2 and Q_4 are produced.

To better grasp the significance of the experimental results, we have also set up MC simulations on a similar system of model particles. By doing so, we initially expected to draw conclusions about the effects of dissipation and nonequilibrium phenomena on the rich behavior presented by the granular monolayer, and the possibility to demonstrate the similarities between the two systems. To generate systems with different packing fractions η, we first initialized the system with a lower packing fraction ($\eta \sim 0.6$), fixing the number of particles to ∼2000 for both circular and square cavities (this is chosen so as to mimic the number of particles in the experiments). Next, we let the simulation run for some time, and then repeatedly try to reduce the size of the container step by step, keeping all particles inside the container. Then, different systems with the desired packing fractions ($\eta \in [0.75, 0.85]$) can be prepared. Once a configuration at the desired density is obtained, we perform 2×10^5 MC steps (MCS), one MCS corresponding to an attempt to move all particles in the system sequentially. As the triangular particles used in the simulations interact through overlap forces, standard MC simulations using the Metropolis *et al.* algorithm are performed, moving and rotating particles at random at each step, by rejecting overlapping configurations and only accepting nonoverlapping ones, which asymptotically generates a Boltzmann distribution. Measurement of the relevant quantities explained in Sec. IV is made every 500 MCS, totaling 400. Translational and rotational amplitudes (maximum displacement or angle a particle can be displaced or rotated) are monitored and changed to target an acceptance probability of 0.35. Particle movements are set up so that on one-third of the times particles are only translated, on another third particles are only rotated, and in the rest both movements are made simultaneously.

IV. RESULTS AND DISCUSSION

We present results for the circular and square cavities separately. In both cases, a range of packing fractions was explored, spanning most of the stability window of the 6-atic liquid crystal. In order to identify and characterize the different configurations in which particles can be arranged, we need some way to determine the orientational order of the system. First, we define three orientational order parameters, $Q_n = |\langle e^{in\phi}\rangle|$, $n = 2, 4, 6$, that probe two-, four- and sixfold symmetries, respectively. ϕ is the angle between the particle axis and a fixed reference frame, for instance, the x axis of the laboratory's reference frame. The angular brackets indicate that we take the average in a circular region of radius $4s$ centered on a particle. We measure this quantity on each particle of the system. This expression of the order parameters follows from the second-rank tensor $\hat{Q} = \langle 2\boldsymbol{e} \otimes \boldsymbol{e} - \mathbb{1}\rangle$ of the nematic phase (with $\boldsymbol{e}$ the unit vector pointing along the particle axis). The nematic director of uniaxial rods can be found by computing the eigenvector corresponding to the maximum eigenvalue of this tensor. For particles with two (squares) or three (equilateral triangles) equivalent axes, generating the 4-atic or 6-atic phases, respectively, the orientational-order tensors are defined similarly, but they are of four and six ranks, respectively [37]. The procedure to find the directors is exactly the same: the calculation of the eigenvectors corresponding to the maximum eigenvalues of properly contracted tensors to obtain a second-rank tensor [37]. In turn, the maximum eigenvalue is the order parameter. Following this procedure, one can find that the maximum eigenvalue for the 6-atic symmetry is just $Q_6 = [\langle\cos 6\phi\rangle^2 + \langle\sin 6\phi\rangle^2]^{1/2} = |\langle e^{6i\phi}\rangle|$. Note that these order parameters are defined locally at each particle. The calculation of the order parameters is made for both the granular experiments and the MC simulations.

A. Circular cavity

Figure 4 shows representative color maps of the three order parameters, from experiment and simulation, for two different values of packing fraction. After a short equilibration time, a clear 6-atic phase is stabilized in the system in the steady state (low values for the Q_2 and Q_4 order parameters, and a high value of Q_6). As expected, geometric frustation causes the system to develop six defects of charge $q = +1$, giving a total charge $q_t = +6$. These defects, being positive, repel each other through the orientational stiffness of the 6-atic fluid, and are located very close to the inner wall of the cavity approximately at the vertexes of a hexagon inscribed in the cavity. This structure is subject to global rotation, as is typical in vibrated monolayers. Figure 5(a) shows an example of a

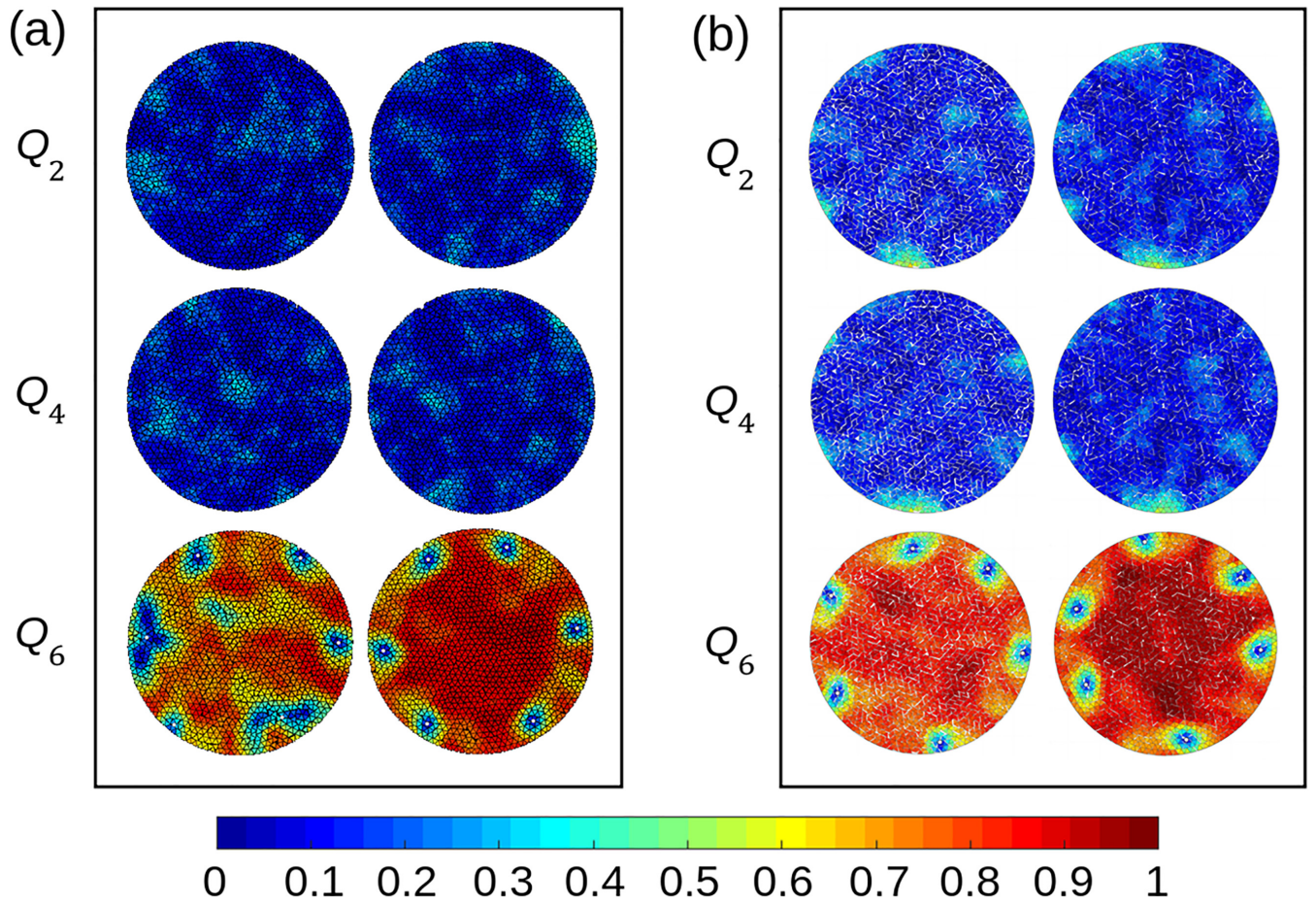


FIG. 4. Order parameters. (a) Experiments, $\eta = 0.78$ (left) and 0.85 (right). (b) Simulations (same packing fractions). Value of the order parameters are indicated in the color bar.

distribution of the radial positions of the defects, which is a sharply peaked function located at $r \simeq 0.9L/2$.

As a complementary calculation, we have simulated a fluid of 2D hard triangles using MC technique. Properties of the granular monolayers are reproduced in the MC simulations, demonstrating that, despite their dissipative nature, the basic physics of the behavior of the granular quasimonolayer can be understood in terms of excluded-volume particle interactions, which create oriented fluids and a stiff but deformable director field, much as in their thermal-equilibrium counterparts. This

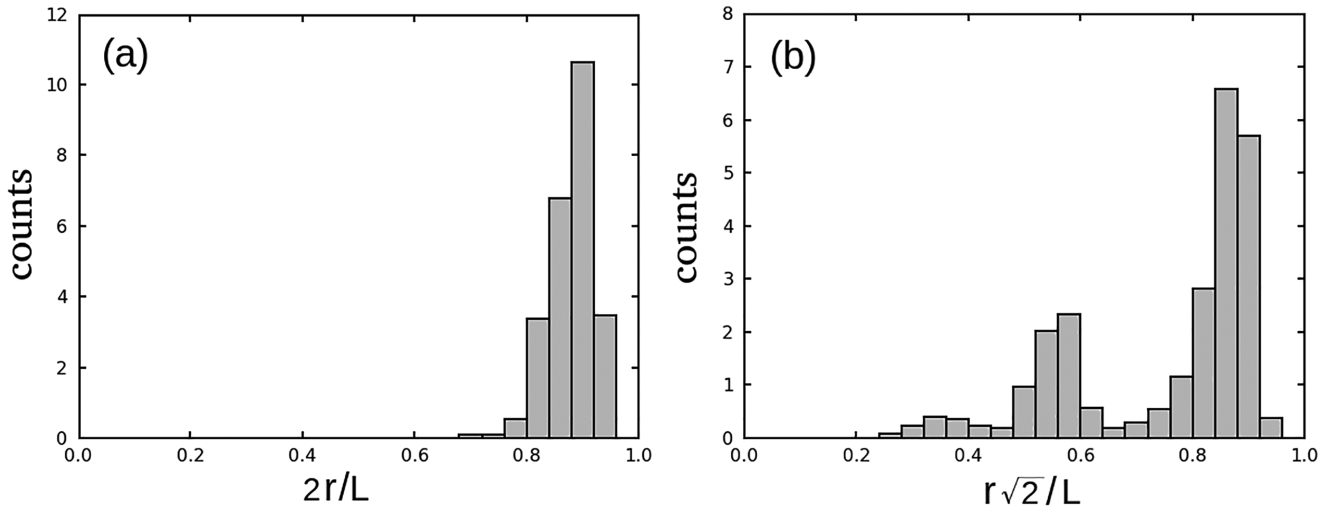


FIG. 5. Histograms of defect positions. (a) Circular cavity, using the radius of the cavity $L/2$ as the unit of length. (b) Square cavity, using half of the cavity diagonal $L/\sqrt{2}$ as the unit of length.

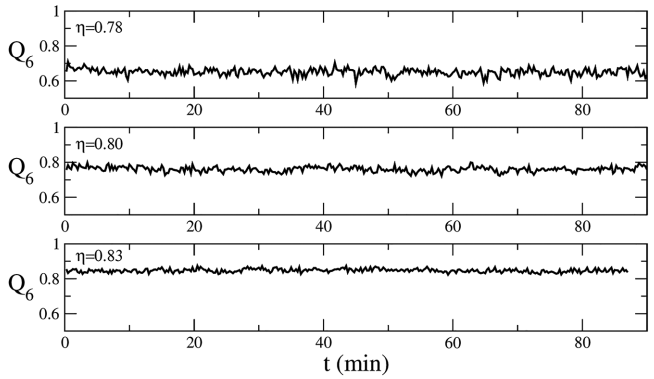


FIG. 6. Time evolution of Q_6 in the steady states of runs with different values of packing fraction (indicated in each graph).

is demonstrated in Fig. 4, which compares particle configurations in the granular and thermal system for two different densities.

Figure 7 shows the behavior of the order parameters Q_n with packing fraction in the granular monolayer. As expected from the sixfold symmetry of the particle, the order parameters Q_2 and Q_4 are vanishing small, while Q_6, a direct measure of the 6-atic ordering, saturates at values $\sim$0.85 when packing fraction is close to 0.9 (note that the crystal phase expected at such high values of packing fraction does not appear in our experiments since the boundary conditions imposed by the circular confinement are incompatible with the triangular or hexagonal symmetries of the crystalline lattices). As usual Q_6 decreases as η is lowered but with an interesting behavior: Instead of having a relatively abrupt change close to the isotropic to 6-atic phase transition as in equilibrium systems, it decreases with a rather small slope to values clearly different from zero. This behavior is due to the dissipative nature of the system, which promotes the presence of a large proportion of clusters formed by hexagonal aggregates of triangles. In regions where clusters are present, the order parameter Q_6 is relatively high, resulting in a total averaged value (over the whole sample) of Q_6 appreciably different from zero.

B. Square cavity

As explained above, in both circular and square cavities an initial equilibration run, lasting $\sim$1 h, is done, after which a second run is run and used to take averages. The start of the latter, which we assign to a steady-state condition, is defined as the time from which the values of Q_6 clearly start to fluctuate about a stable mean value. Figure 6 shows the time evolution of Q_6 for a number of experimental runs with different densities during the steady states for the square cavity. In all cases, no overall drift is detected, but fluctations about the mean value increase as the density is lowered.

Steady-state configurations in the square cavity also comply with the rules of topology, but there are some features that are not seen in the circular cavity. We start with Fig. 7, which shows the evolution of Q_n with η. It is interesting to note that at high density the square confinement enhances the 6-atic ordering as compared with its circular counterpart. This is due

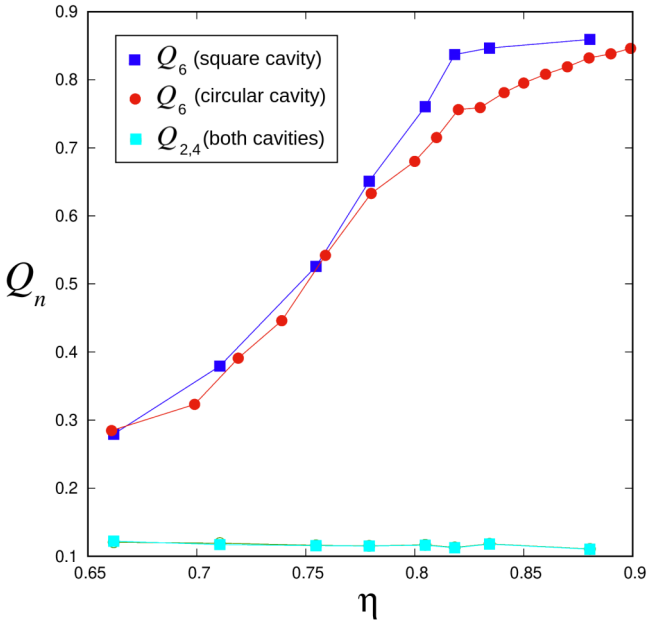


FIG. 7. Order parameters Q_n, averaged over the whole cavity, as a function of the packing fraction η in monolayers of equilateral triangular prisms confined in circular (circles) and square (squares) cavities. Note that order parameters Q_n with $n = 2, 4$ (for both cavity shapes) are relatively small (close to 0.1). Each symbol represents a single experiment, totaling 17 experiments for the circular cavity and 8 experiments for the square cavity.

to the strong anchoring effect of the square walls promoting a perfect orientation of triangles belonging to the first few monolayers in contact with the walls of the square. For the circular cavity, the orientations of triangles at contact with the circular wall have a continuous variation due to the curvature of the container.

The distinct nature of the defects in the square cavity is shown in Fig. 8, which depicts representative maps of Q_6. In this case, six defects are excited, as in the circular cavity,

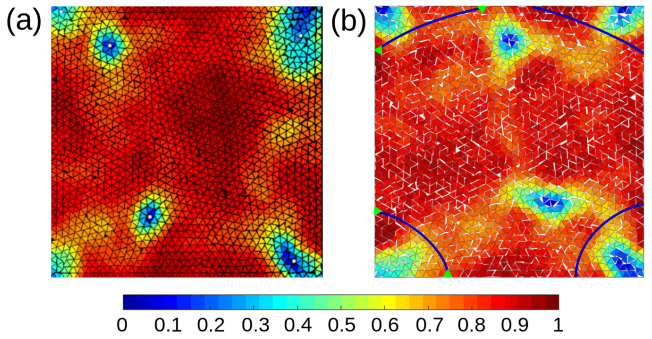


FIG. 8. Comparison between configurations of triangular prisms in the square cavity as obtained from (a) granular monolayers (packing fraction $\eta = 0.82$) and (b) MC simulations ($\eta = 0.85$). In both cases, two $+2$ charges are found in the square corners at the bottom, while two $+1$ charges are at the upper corners (cf. Fig. 9). Free defects with charges $+1$ and -1 are located in the bulk of the system (cf. Fig. 1). Approximate director lines around pinned defects of charges $+2$ and $+1$ are depicted. Colors indicate the value of Q_6.

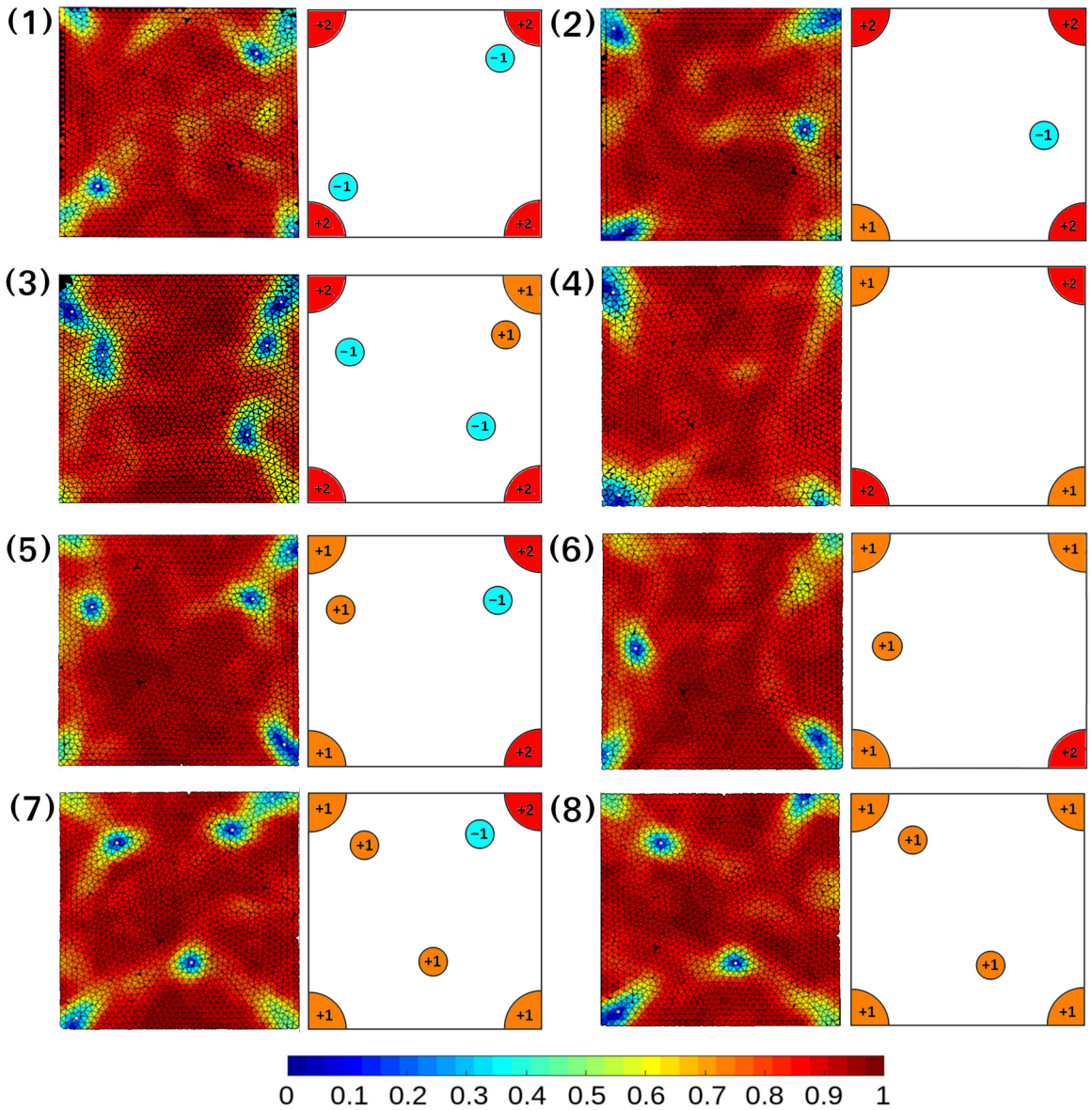


FIG. 9. The different defect structures exhibited by the granular monolayer. The labels 1–8 correspond to the configurations collected in Table I. Colors indicate the value of Q_6.

but not all defects have the same nature. We can distinguish two types of defects. One type corresponds to *pinned* defects, found in or close to the four corners of the cavity, which present no motion. These defects are always present as the corners are not compatible with a continuous director field with 6-atic symmetry. The other type of defects correspond to *free* defects, which are excited in the bulk of the cavity and are not static but in fact very dynamic. Free defects may appear in number as none, one, two, or three (in Fig. 8 two free defects are visible, both in the granular quasimonolayer and in the MC simulations). The approximately bimodal radial distribution of defects, shown in Fig. 5(b), reflects the existence of a strongly located population close to the corners of the cavity (pinned defects), along with a group of defects more loosely located in the bulk of the cavity (free defects). The slightly localized nature of the latter may reflect their relatively strong interactions with the pinned defects.

One important feature of this system is that defects may have different charges, some of them even with different signs, and therefore the system may exhibit repelling and attractive defect pairs. It will prove useful to designate different configurations by listing the set of their charges. In the following, a given configuration of defects will be denoted by a list of all the defect charges, starting with the pinned ones (indicated by a subscript "p") and followed by the free defects (subscript "f"). To shorten notation, negative charges will be underlined. Thus, the configurations shown in Fig. 8 are both denoted by $2_p 2_p 1_p 1_p 1_f \underline{1}_f$. Note that this notation does not distinguish between the cases where the two $+2$ charges are along the square diagonal or at the same side of the square.

Figure 9 presents a summary of all eight structures found in the granular system. Representative configurations of the granular system are shown, together with schematics depicting the charge and location of the defects in the images of

TABLE I. Different defect structures containing four pinned defects and a number of free defects observed in the granular monolayer. The configuration number corresponds to the number assigned in Fig. 9. Pinned charges are indicated with a "p" subscript, whereas an "f" subscript refers to free charges. Negative charges are underlined. Note that configuration 4 displays no free charges. The fourth column collects the elastic free energy in units of πK from Eq. (6) corresponding to configurations of Fig. 9, while the fifth column collects the minima of the elastic free energy from the same equation where the distances between charges were taken to be greater than or equal to $2a$. The configurations corresponding to these minima are shown in Fig. 10. Configuration 5′ is not found in the experiments, and refers to a charge distribution similar to that of configuration 5 in terms of location of pinned and free charges, but with pinned charges of +2 located opposite along the diagonal of the cavity (see Fig. 9). According to elastic theory, the free energy of configuration 5′ is lower than that of configuration 5.

Conf.	Charges (pinned)	Charges (free)	$\mathcal{F}_{\rm el}$ (πK)	$\mathcal{F}_{\rm el}^{\rm (min)}$ (πK)
1	$2_p\ 2_p\ 2_p\ 2_p$	$\underline{1}_f\ \underline{1}_f$	1.3548	1.3140
2	$2_p\ 2_p\ 2_p\ 1_p$	$\underline{1}_f$	1.3268	1.2745
3	$2_p\ 2_p\ 2_p\ 1_p$	$\underline{1}_f\ \underline{1}_f\ 1_f$	1.3280	1.2564
4	$2_p\ 2_p\ 1_p\ 1_p$	0_f	1.2365	1.2365
5	$2_p\ 2_p\ 1_p\ 1_p$	$1_f\ \underline{1}_f$	1.2825	1.2300
5′	$2_p\ 2_p\ 1_p\ 1_p$	$1_f\ \underline{1}_f$	X	1.2197
6	$2_p\ 1_p\ 1_p\ 1_p$	1_f	1.2208	1.2048
7	$2_p\ 1_p\ 1_p\ 1_p$	$1_f\ 1_f\ \underline{1}_f$	1.2708	1.1848
8	$1_p\ 1_p\ 1_p\ 1_p$	$1_f\ 1_f$	1.2209	1.1676

the granular monolayers. Table I shows these combinations of pinned and free defects for the different configurations, along with their charge designations. The conservation of total topological charge requires the charge of the individual defects to be correctly interpreted in all cases where varying numbers of defects are present. An important point is that, from the analysis of Sec. II, all eight types of configurations can be explained in terms of four pinned defects at the corners of the cavity, with charges +2 or +1, and free defects in varying numbers with charge ±1. In this way, all configurations satisfy the requirement of the total topological charge being $q_t = +6$. As mentioned previously, the identification of defect charges can be made from the geometry of the director field in the neighborhood of the defects. Thus, as shown in Fig. 8, pinned defects of charge +2 are identified by director lines that are concave with respect to its corner, while pinned defects of charge +1 exhibit distinctive convex director lines. Free defects can similarly be identified by lines forming convex pentagonal shapes (charge +1) and nonconvex, heptagonal shapes (charge −1).

To see whether we can rationalize this phenomenology in terms of the effective free energies implied by elastic theory, we consider the elastic interaction energy [Eq. (6)] and a simplified model for defect cores. Assuming defect cores to behave as hard particles of diameter $2a$, we can search for the minimum-energy position of free charges in each configuration, keeping the pinned charges at the corner positions. We explore the multiparametric space of the coordinates (x_i, y_i), $i = 1, \ldots, n$, with n the number of free charges in each configuration, both using a discrete grid and alternatively using an MC sampling scheme. Note that we assume pairwise interactions, and do not try to model specific interactions between defects at short distances, which would require the minimization of a full elastic model taking defects as singularities of the local orientation field. The results from the simplified elastic model does not fully grasp the fine details of the granular configurations, but help understand the defect configurations.

Table I shows values of the elastic free energy of configurations of charges shown in Fig. 9. Also, it is collected in the same table the minimum-energy charge configuration, obtained by minimizing the elastic free energy of the corresponding N-defect systems using Eq. (6). The parameters have values $R = 2L$ (with L the edge length of the square cavity) and $a = 0.1L$. Pinned defects are taken to be static and have been located at the vertexes of the cavity. The ordering of the free energies (from lower to higher) corresponding to defect configurations from Fig. 9 produces the sequence $6 \to 8 \to 4 \to 7 \to 5 \to 2 \to 3 \to 1$. However, the ordering of the minimum free energies produces the following one: $8 \to 7 \to 6 \to 5 \to 4 \to 3 \to 2 \to 1$, implying that the free energy is higher when the number of +2 charges is larger. Figure 10 presents a schematic diagram with the location of charges in the minimum-energy configurations. In general, when a negative free charge is present, it sticks close together to one of the pinned +2 charges. If, in addition to the negative free charge, there is a positive charge, the two stick together. When all pinned charges have a charge of +2, the two negative free charges stay in contact with two pinned charges located at one of the square diagonals, with their centers of mass positioned close to the diagonal. Finally, when all the charges have positive +1 charge, free charges are located midway between a pair of pinned charges along one of the sides of the square, and one in front to the other. Therefore, in most cases defects are located close to or at the sides of the square.

As regards the similarities between experiment and theory as far as the position of free defects is concerned, a simple comparison between Figs. 9 and 10 shows that configurations 1 and 6 are very similar. As a general rule, experiment and theory both exhibit configurations where negative free charges are very close to a pinned defect of charge +2. However, the predicted tendency of defects to be close to the boundaries according to elastic theory does not hold in the case of experiments (see Fig. 9), where free charges tend to be in the bulk of the cavity, far from the boundaries. This difference can be explained by the presence of layers of triangles close to the walls featuring strong crystalline ordering (due to the strong anchoring conditions at the walls), which reflects in an effective repulsive interaction between these layers and the

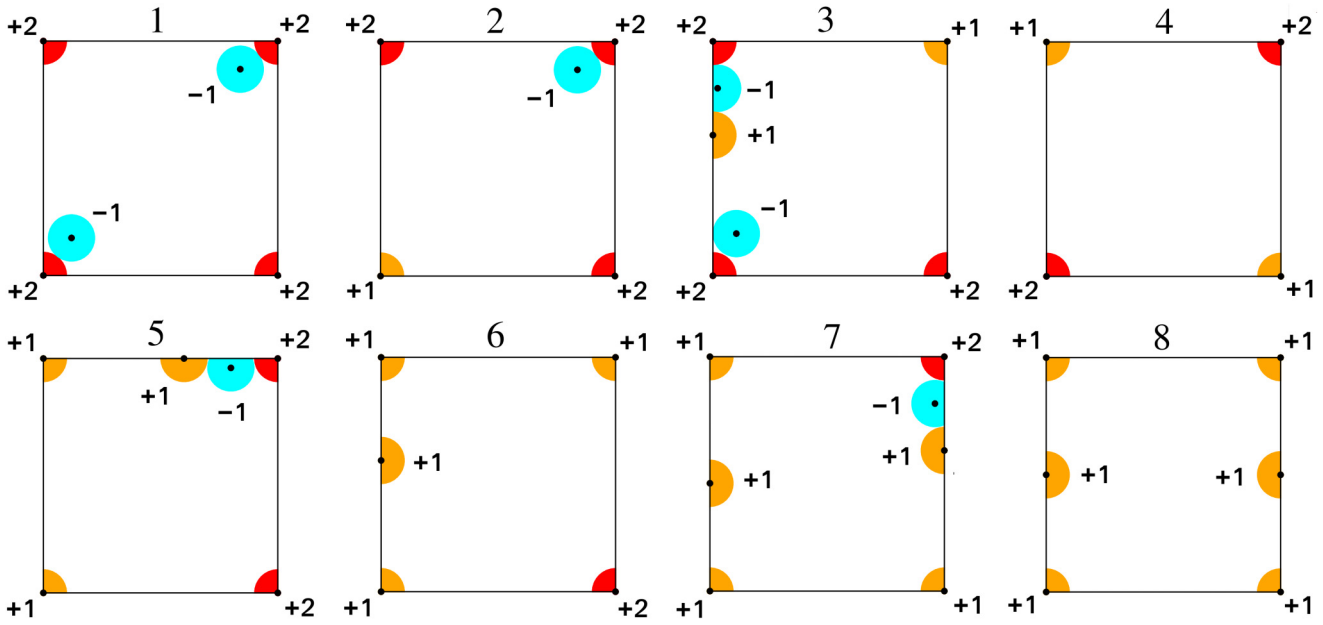


FIG. 10. Equilibrium distribution of charges obtained from the minimization of Eq. (6) selecting $R = 2L$ and $a = 0.1L$ (similar to the core size observed in the experiments, defining the latter as that of the region where $Q_6 < 0.4$), with pinned and free charges being those of configurations shown in Fig. 9. The pinned charges are always located at the vertexes of the square and we selected $2a$ as the minimum distance between any two charges.

defects, a fact not taken into account by the model. Also, when a negative free charge is present, the minimum free-energy configuration predicted by the elastic model is that corresponding to the coalescence of the negative charge with one +2 pinned charge, except when certain constraint for a minimum distance between charges is imposed, something that we have done by assuming $r_{ij} \geqslant 2a$. In experiments, negative charges are close to the +2 charges most of the time, but can travel to relatively distant positions (see configuration 2 in Fig. 9).

Note that the configurations of the granular monolayers shown in Fig. 9 do not necessarily correspond to minimum-energy configurations since free defects are very dynamic and, as discussed below, undergo fusion and disintegration events, which make the system to transit from one to another of the typical configurations shown in Table I. Also, the elastic model only represents an approximation to the real physics, and minimum-energy configurations for a system with a particular number and distribution of charges may not necessarily be related to the actual typical or average configuration with the same charges. In particular, the pair interaction model implicit in Eq. (6) may not be correct, particularly at short distances, as interactions between defects are mediated by the rigidity of the 6-atic underlying phase, and collective interactions are expected.

Not only do different defect configurations stabilize in the system, but we observe a fast dynamics between different types of configurations, meaning that these defects can undergo processes of fusion and splitting, and that the system can visit multiple configurations (see Table I). Several such elemental events can be seen in a given run. For example,

$$\begin{aligned} &7 \longleftrightarrow 8 \quad \text{and} \quad 5 \longleftrightarrow 6 \quad (+2_{\mathrm{p}} - 1_{\mathrm{f}} \longleftrightarrow +1_{\mathrm{p}}), \\ &5 \longleftrightarrow 7 \quad (+2_{\mathrm{p}} \longleftrightarrow +1_{\mathrm{p}} + 1_{\mathrm{f}}), \\ &6 \longleftrightarrow 7 \quad (0_{\mathrm{f}} \longleftrightarrow +1_{\mathrm{f}} - 1_{\mathrm{f}}), \\ &\ldots \end{aligned} \tag{10}$$

Many of these transitions between different system states occur in a single run, but they only affect the local value of the order parameter, having no impact on the global value shown in Fig. 6.

The histogram of the fraction of time spent in the different configurations is shown in Fig. 11(a). This is a measure of the degree of stability of each configuration. Time refers to physical time, but the histogram is normalized to unity. Fractions of time have been calculated by averaging results for runs with packing fractions in the interval 0.82–0.88, since in this range defects are very compact and the results hardly vary with respect to density. Note that the values of Q_6 for densities in this interval are very similar.

Clearly configurations 4, 6, and 8 are the most stable. We believe this is a robust result of our experiments, which in turn is consistent with the theoretical results. The remaining configurations have short fractions of time, which may be compatible with transition states. The network diagram shown in Fig. 11(b) contains elemental "reactions" between different configurations found in the experiments. The nodes represent the configurations, with their area being proportional to the fraction of time of the specific configuration. The links between the nodes represent the (reversible) transitions between them, and their width is made proportional to the number of transitions between the corresponding states found in the experiments. The numbers attached to each line give the number of transitions detected in the experiments (the first referring to the $n \to n+1$ transitions, the second to the $n+1 \to n$ transitions). Dashed links joining states 1 and 3, and 3 and 5, indicate that, even though these transitions are possible in principle, they have not been found in our experiments

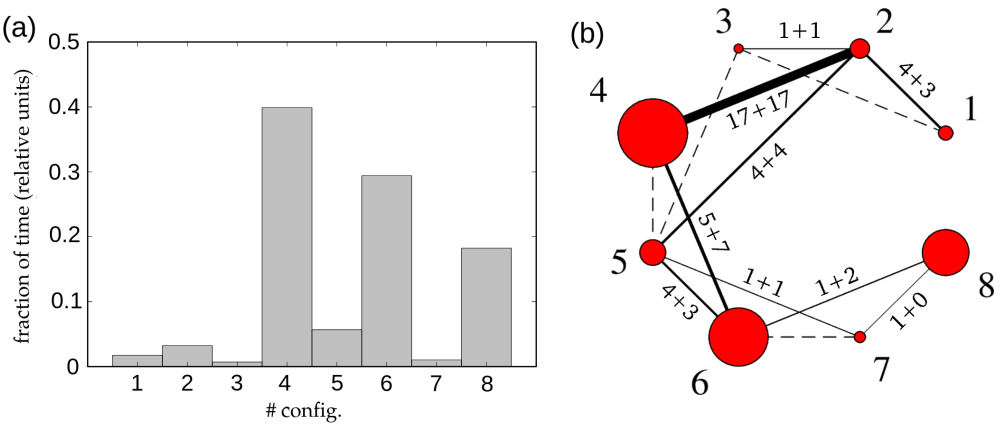


FIG. 11. (a) Histogram of the fraction of time spent in each configuration (in relative units). (b) Network diagram representing different configurations (nodes) of topological charges in the square cavity, along with transitions (links) between them. The area of nodes is proportional to the fraction of time of the configuration, while the width of the links indicates the relative number of (reversible) reactions between a given connected pair of nodes. Dashed links indicate possible transitions not found in our experiments. The numbers attached to each line give the number of transitions detected in the experiments (the first referring to the $n \to n+1$ transitions, the second to the $n+1 \to n$ transitions).

(probably due to their finite duration). A possible explanation is the short fraction of time of configuration 3. The diagram of panel (b) shows that configuration 4 (without free charges) is the most stable in terms of the fractions of time of configurations 6 and 8. Note that configuration 4 has no free charges (see Fig. 9), while configurations 6 and 8 do not exhibit the presence of negative free charges, a result that agrees with elastic theory in that the presence of negative charges is energetically penalized.

Table II contains all possible elemental "reactions" in terms of starting and ending configurations. Most of these events can be seen in the experiments as shown in Fig. 11(b). The persistence of a given configuration has also be quantified. The relatively fast dynamics between defect configurations imply that the charges easily react between them. We have even observed events where charges of the same sign ($+1_{\rm f}$ and $+1_{\rm p}$) fuse together to give a pinned defect of higher charge ($+2_{\rm p}$):

$$8 \longleftrightarrow 6 \quad (+1_{\rm p} + 1_{\rm f} \longleftrightarrow +2_{\rm p}). \tag{11}$$

This process might be possible due to the long-range repulsive interactions due to the rest of charges, which push the free $+1_{\rm f}$ charge against the pinned $+1_{\rm p}$ charge. It would mean that the system may exist in a number of equally metastable configurations with respect to some effective free energy. Also, we observe some correlation between the positions of the $+2_{\rm p}$ pinned charges. In configuration 4, no free charges are excited, and $+2_{\rm p}$ defects are located at opposite corners of the cavity, due to their high repulsion. Two $+2_{\rm p}$ defects may occupy adjacent corners, but only when a $-1_{\rm f}$ free defect screens the interaction (see configuration 5).

The MC simulations exhibit a defect configuration that is similar to one of the configurations found in the granular monolayer. Figure 8 shows a comparison between the two, with the same defect configuration $2_p 2_p 1_f \underline{1}_f$. However, defect "dynamics" is very slow in the simulations, and we have not been able to detect large defect difusion and consequently fusion or disintegration events. This prevents from drawing any conclusion as to the effect of dissipation in the defect dynamics described.

V. CONCLUSIONS

Topology predicts that the total charge in a 6-atic phase confined within circular and square cavities should be the same, $q_{\rm t} = +6$, since a circle and a square share the same topological properties. Vibrated granular monolayers indeed conform to this prediction. However, the distribution of defects—specifically their number and charge—differs

TABLE II. Matrix of elemental "reactions" between the configurations. The symbol "X" indicates that there is no pathway between the corresponding configurations. Labels in gray correspond to possible reactions that have not been detected in our experiments.

Conf.	1	2	3	4	5	6	7	8
1	X	$2_{\rm p}\underline{1}_{\rm f} \to 1_{\rm p}$	$2_{\rm p} \to 1_{\rm p}1_{\rm f}$	X	X	X	X	X
2	$1_{\rm p} \to 2_{\rm p}\underline{1}_{\rm f}$	X	$0_{\rm f} \to 1_{\rm f}\underline{1}_{\rm f}$	$2_{\rm p}\underline{1}_{\rm f} \to 1_{\rm p}$	$2_{\rm p} \to 1_{\rm p}1_{\rm f}$	X	X	X
3	$1_{\rm p}1_{\rm f} \to 2_{\rm p}$	$1_{\rm f}\underline{1}_{\rm f} \to 0_{\rm f}$	X	X	$2_{\rm p}\underline{1}_{\rm f} \to 1_{\rm p}$	X	X	X
4	X	$1_{\rm p} \to 2_{\rm p}\underline{1}_{\rm f}$	X	X	$0_{\rm f} \to 1_{\rm f}\underline{1}_{\rm f}$	$2_{\rm p} \to 1_{\rm p}1_{\rm f}$	X	X
5	X	$1_{\rm p}1_{\rm f} \to 2_{\rm p}$	$1_{\rm p} \to 2_{\rm p}\underline{1}_{\rm f}$	$1_{\rm f}\underline{1}_{\rm f} \to 0_{\rm f}$	X	$2_{\rm p}\underline{1}_{\rm f} \to 1_{\rm p}$	$2_{\rm p} \to 1_{\rm p}1_{\rm f}$	X
6	X	X	X	$1_{\rm p}1_{\rm f} \to 2_{\rm p}$	$1_{\rm p} \to 2_{\rm p}\underline{1}_{\rm f}$	X	$0_{\rm f} \to 1_{\rm f}\underline{1}_{\rm f}$	$2_{\rm p} \to 1_{\rm p}1_{\rm f}$
7	X	X	X	X	$1_{\rm p}1_{\rm f} \to 2_{\rm p}$	$1_{\rm f}\underline{1}_{\rm f} \to 0_{\rm f}$	X	$2_{\rm p}\underline{1}_{\rm f} \to 1_{\rm p}$
8	X	X	X	X	X	$1_{\rm p}1_{\rm f} \to 2_{\rm p}$	$1_{\rm p} \to 2_{\rm p}\underline{1}_{\rm f}$	X

significantly between the two geometries. This difference arises due to the presence of corners in the square cavity, which anchor two distinct types of defects. We have demonstrated that these static defects can have charges $q = +1_p$ or $q = +2_p$, and multiple charge combinations are possible. However, only one combination, $q = \{+2_p, +2_p, +1_p, +1_p\}$, is free from defects in the bulk and in fact the most frequently seen configuration in the experiments, probably being the most stable.

When the sum of the charges of the pinned defects is less than +6, free defects are excited in the bulk of the cavity to restore charge conservation. These free defects can have charges $q = \pm 1_f$, which means that both positive- and negative-charge defects can be excited in the system. The coexistence of positive and negative charges in the system leads to fast dynamics, with rapid transitions between different configurations. The elastic model explains this by showing that configurations with different charge numbers have nearly equivalent elastic free energies. This does not imply that the free-energy barriers are particularly high or low; rather, experimental findings suggest that the barriers are relatively low, facilitating the fusion and disintegration of defects within the system.

The softness of this granular system arises from the presence of 6-atic orientational order within an otherwise fluid monolayer, as well as from the pinning effects of the sharp, right-angled corners of the cavity. These corners anchor two distinct types of pinned defects with charges +1 and +2. This is in contrast with the circular cavity, where only +1 free charge defects are excited. The unique geometry of the square cavity, combined with the sixfold orientational order in the fluid, provides an ideal setting for studying defect dynamics. While nonequilibrium processes, such as friction and dissipation, likely contribute to the fast defect dynamics observed, we have been unable to fully analyze their impact through comparison with equilibrium MC simulations.

Our results may open up an avenue in the study of defect configurations in confined liquid-crystalline systems and the effect of the geometry of the container, such as general n-sided regular or nonregular polygonal cavities. Some ideas related to defect configurations in systems of equilateral triangular particles confined in n-sided regular polygonal cavities are provided in the Appendix. In particular, we provide a general procedure to predict the number of different configurations of topological charges inside a polygonal cavity of n sides. Assuming that each vertex can admit only positive charges +1 or +2, and that the total number of free negative charges inside a cavity (with a size approximately equal to the experimental one) cannot be greater than two, we can predict the number of possible configurations. As the number of polygonal sides increases, repulsive interactions between neighboring pinned charges could force the latter to transform to domain walls (separating regions with depleted orientational ordering from regions with different director orientations). This scenario will be the subject of future research lines.

ACKNOWLEDGMENTS

Financial support from Grants No. PID2023-148633NB-I00/AEI and No. PID2021-126307NB-C21/MICIU/AEI/10.13039/501100011033/FEDER,UE is acknowledged. Ariel Díaz de Armas is gratefully acknowledged for his contributions to the software used in this work.

DATA AVAILABILITY

The data that support the findings of this article are openly available [38], embargo periods may apply.

APPENDIX: EQUILATERAL TRIANGULAR PRISMS CONFINED IN POLYGONAL CAVITIES

In this Appendix, we have investigated the ordering properties of a fluidized monolayer of equilateral triangular prisms confined within two types of cavities: a square cavity (with $n = 4$ sides) and a circular cavity, which can be considered the limiting case of a regular polygon with $n \to \infty$ sides. Although both cavities share the same topological characteristics, namely, the same total topological charge, we have found that the nature and spatial distribution of topological defects differ significantly between them.

This observation naturally raises the question: How does the distribution of defects evolve as the number of sides n increases, and is there a critical value of n beyond which the system exhibits the same behavior as in the circular cavity, characterized by six free defects each with topological charge +1? To address this, the present Appendix explores the general case of a regular polygonal cavity with arbitrary n, aiming to understand the crossover between polygonal and circular confinement.

We begin by demonstrating that defects are expected to form at the vertices of a polygonal cavity, and that only two types of defects can arise, with topological charges $q = +1$ and +2. To understand this, consider two adjacent linear boundaries that meet at a vertex of an n-sided polygon. Due to packing considerations, a well-ordered monolayer tends to form along each boundary, consisting of triangles arranged in an alternating pattern. In this configuration, particles adopt two distinct orientations: one where a triangle aligns with a side in contact with the boundary ("type 1"), and another where a vertex of the triangle touches the boundary ("type 2"); see Fig. 12(a). Note that the interior angle at the vertex of a regular n-sided polygon is $\alpha = \pi - 2\pi/n$.

As one moves from the horizontal boundary to the oblique one following a director line joining triangles of the same type, the particle axis rotates $\alpha - \pi/3 = 2\pi/3 - 2\pi/n$ counterclockwise. See Fig. 8(b), where relevant director lines joining triangles at the boundaries for the pinned defects are depicted. For triangles of different types, the rotation angle is $\alpha - 2\pi/3 = \pi/3 - 2\pi/n$, clockwise for $n < 7$ and counterclockwise for $n \geqslant 7$ [see Figs. 12(b) and 12(c)]. Both rotations are interior; i.e., they take place close to but not at the polygonal vertex. Right at the vertex the rotation angle is $2\pi/n$, so that the total (accumulated) rotation angle is $2\pi/3$ and $\pi/3$, respectively. The associated winding numbers of defects pinned at the vertices of the n-sided polygon are then

$$k = \frac{(2\pi/3)}{2\pi} = \frac{1}{3} \quad (\text{charge } q = pk = +2),$$
$$k = \frac{(\pi/3)}{2\pi} = \frac{1}{6} \quad (\text{charge } q = pk = +1), \qquad \text{(A1)}$$

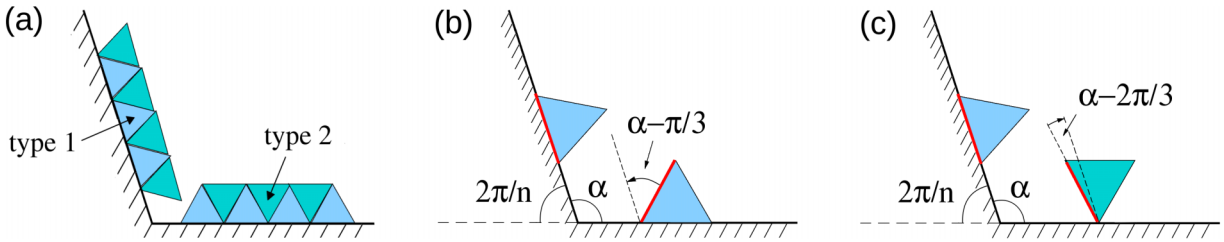


FIG. 12. (a) Schematic of two monolayers of equilateral triangles in contact with two consecutive walls of a polygonal cavity. Triangles with different orientations with respect to the walls have been indicated as "type 1" and "type 2." (b), (c) Rotation of a triangle close to a vertex of an n-sided confining polygon. In panel (b), the type is invariant under rotation, while in panel (c) the type changes.

where we set $p = 6$ as appropriate for a 6-atic symmetry. It is important to note that for $n = 3$ (triangular cavity) and $n = 6$ (hexagonal cavity) triangles of the same (different) types rotate 0 $(-\pi/3)$ and $\pi/3$ (0), respectively, implying that no defects are present in these cavities. For other polygonal confinements, defects of topological charges $+1$ and $+2$ will be present.

Let us now consider the contribution of free charges. In an n-sided polygonal cavity, the sum of m_1 pinned defects with charge $+1$ and m_2 pinned defects with charge $+2$ must satisfy the condition $m_1 + m_2 = n$. In the presence of j_1 and j_{-1} free charges with values $+1$ and -1, respectively, the overall topological charge conservation leads to

$$m_1 + 2m_2 + j_1 - j_{-1} = 6 \quad \Rightarrow \quad 2n + j_1 - m_1 - j_{-1} = 6. \tag{A2}$$

In the specific case of a square cavity ($n = 4$), this condition simplifies to

$$2 + j_1 = m_1 + j_{-1}. \tag{A3}$$

By examining all possible values of m_1 in the range 0–4, we can identify the corresponding pairs (j_1, j_{-1}) that satisfy the charge balance equation. These combinations yield the distinct configurations of pinned and free charges that have already been discussed in detail in Sec. IV B 1.

Our analysis is restricted to configurations involving no more than three free charges, as configurations with higher numbers are highly unlikely in our system. This limitation stems from the fact that the cavity size is comparable to the extrapolation length of the liquid-crystalline 6-atic phase. Indeed, such excess charges are not observed in experiments. However, larger cavities could in principle support a greater number of free charges.

This approach can be extended beyond the square cavity. For instance, in the case of a pentagonal cavity ($n = 5$), the charge conservation equation becomes

$$4 + j_1 = m_1 + j_{-1}. \tag{A4}$$

Applying the same reasoning and again restricting the number of free charges to at most three, we can enumerate all compatible configurations of pinned and free charges. These are summarized in Table III. Among these, configurations 1, 3, and 5 are expected to have the longest fractions of time, as they contain either no free charges or only one, which minimizes the free-energy cost, as discussed previously. Let C denote the total number of defect configurations containing no more than three free defects. This number depends on n, the number of sides of the confining polygon. We also define

$$\mathcal{N} = m_1 + m_2 + j_1 + j_{-1} = n + j_1 + j_{-1} \tag{A5}$$

as the total number of defects (both pinned and free) of a given configuration, again under the constraint that there be at most three free defects. The value of $\mathcal{N}$ varies between a minimum and a maximum, given by

$$\mathcal{N}_{\min} = \max(n, 2n - 6) \ \text{ and } \ \mathcal{N}_{\max} = n + 3, \tag{A6}$$

for $n \leqslant 9$. These bounds represent the smallest and largest possible total numbers of topological charges in the allowed configurations. Table IV summarizes the values of C, $\mathcal{N}_{\min}$, and $\mathcal{N}_{\max}$ as a function of n. The cases $n = 3$ and $n = 6$ are excluded from consideration, as these geometries do not induce topological defects, as previously discussed. For $n \geqslant 10$, all possible configurations necessarily involve more than three free defects and are therefore beyond the scope of our analysis.

As the number of the sides of a polygon inscribed in a circle of fixed radius increases, the elastic energy contribution from the pinned defects, each carrying a positive charge, also increases, due to their mutual repulsion. To maintain the total topological charge at $+6$, an increasing number of negatively charged free defects must emerge to compensate for the growing excess of positive charge concentrated at the corners of the cavity. However, configurations involving negative free defects tend to have reduced fractions of time, as previously discussed. For these reasons, we expect that, beyond a certain critical number of sides, likely equal to $n^* = 10$ (see Table IV), the system will transition from a polygonal to an effectively circular confinement. In this regime, the configuration consists of six free defects, each with charge $+1$, consistent with the known behavior in circular geometries.

TABLE III. Defect configurations (assuming no more than three free charges) inside a pentagonal ($n = 5$) cavity consisting of m_1 pinned defects of charge $+1$, m_2 pinned defects of charge $+2$, j_1 free defects of charge $+1$, and j_{-1} free defects of charge -1.

Conf.	1	2	3	4	5	6	7	8
m_1	5	5	4	4	3	3	2	1
m_2	0	0	1	1	2	2	3	4
j_1	1	2	0	1	0	1	0	0
j_{-1}	0	1	0	1	1	2	2	3

TABLE IV. Total number of defect configurations C with no more than ten free charges, and minimum $\mathcal{N}_{\min}$ and maximum $\mathcal{N}_{\max}$ number of defects as a function of the number of sides of the polygon, n. The case of a circular cavity, $n \to \infty$, is also included.

n	4	5	7	8	9	10	∞
C	8	8	4	2	1	0	1
$\mathcal{N}_{\min}$	4	5	8	10	12	X	6
$\mathcal{N}_{\max}$	7	8	10	11	12	X	6

This conjecture could be tested in future experimental work planned in our laboratory. It is important to note that these conclusions apply to cavities with dimensions comparable to those used in the present study. For larger cavities, the number of free defects may exceed three, potentially giving rise to a larger number of defects and a richer variety of defect configurations.

Finally, it is fruitful to consider other particle geometries. Triangular particles exhibit a unique characteristic: Perfect monolayers formed on flat surfaces can adopt two distinct configurations—either one vertex or one side in contact with the surface. As a result, when confined in polygonal cavities, such granular fluids develop two types of pinned defects at the corners, with topological charges $+1$ or $+2$. In contrast, particle geometries that allow only a single stable configuration in contact with the cavity walls produce just one type of pinned defect. A paradigmatic case is a granular fluid composed of square particles. Following a director line from one wall to the next (assuming perfect anchoring conditions of squares at both walls) accumulates an interior rotation angle given by $\alpha - \pi/2 = \pi/2 - 2\pi/n$; see Fig. 13(a). The total accumulated rotation includes both this interior rotation and the additional rotation at the vertex, $2\pi/n$, summing to $\pi/2$. The resulting winding number of the defect is then $k = (\pi/2)/(2\pi) = 1/4$. Given the fourfold symmetry of the tetratic phase ($p = 4$), the topological charge is $q = kp = +1$. This leads to a conservation law for the total topological charge within a polygonal cavity of n sides, $n + j_1 - j_{-1} = 4$, where j_1 and j_{-1} denote the number of free defects with charges $+1$ and -1, respectively [see panels (b) and (c) of Fig. 13]. This constraint limits the total number of free defects to $j_1 + j_{-1} \leqslant 3$, under the conditions $m_2 = 0$ and $m_1 = n$ (i.e., all corners are occupied by pinned defects of charge $+1$). Examples of allowable configurations include the following:

(1) $n = 3$ (triangular cavity): There are two possibilities: (i) $j_1 = 1$ and $j_{-1} = 0$, or (ii) $j_1 = 2$ and $j_{-1} = 1$.

(2) $n = 4$ (square cavity): No free defects appear, as the square cavity is compatible with tetratic symmetry.

(3) $n = 5$ (pentagonal cavity): (i) $j_1 = 0$ and $j_{-1} = 1$, or (ii) $j_1 = 1$ and $j_{-1} = 2$.

(4) $n = 6$ (hexagonal cavity): Only one configuration with $j_1 = 0$ and $j_{-1} = 2$.

(5) $n = 7$ (heptagonal cavity): The only configuration has $j_1 = 0$ and $j_{-1} = 3$.

(6) $n = 8$ (octogonal cavity): No configurations satisfy the constraint with three or fewer free charges.

This analysis clearly shows that particles with geometries that allow only a single anchoring configuration, such as squares, form monolayers that, when confined in polygonal cavities, present significantly fewer defect configurations compared to triangular particles.

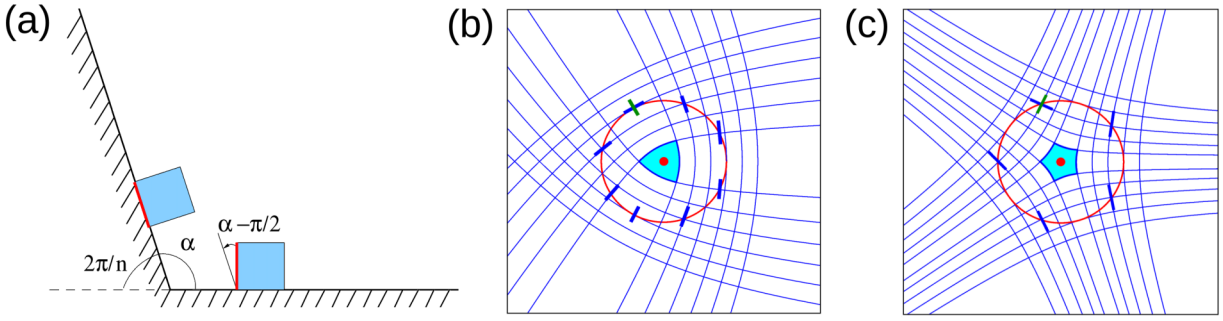


FIG. 13. (a) Schematic of square particles pertaining to perfect monolayers on consecutive sides of an n-sided polygon, representing the positions before and after a rotation by $\alpha - \pi/2$. Curves of director orientations around free defects of winding numbers $+1/4$ [panel (b), charge $+1$] and $-1/4$ [panel (c), charge -1].

[1] A. Kudrolli, M. Wolpert, and J. P. Gollub, Cluster formation due to collisions in granular material, Phys. Rev. Lett. **78**, 1383 (1997).

[2] J. S. Olafsen and J. S. Urbach, Two-dimensional melting far from equilibrium in a granular monolayer, Phys. Rev. Lett. **95**, 098002 (2005).

[3] I. S. Aranson and L. S. Tsimring, Patterns and collective behavior in granular media: Theoretical concepts, Rev. Mod. Phys. **78**, 641 (2006).

[4] E. Khain and I. S. Aranson, Hydrodynamics of a vibrated granular monolayer, Phys. Rev. E **84**, 031308 (2011).

[5] G. Castillo, N. Mujica, and R. Soto, Universality and criticality of a second-order granular solid-liquid-like phase transition, Phys. Rev. E **91**, 012141 (2015).

[6] V. Narayan, N. Menon, and S. Ramaswamy, Nonequilibrium steady states in a vibrated-rod monolayer: Tetratic, nematic, and smectic correlations, J. Stat. Mech. (2006) P01005.

[7] J. Galanis, D. Harries, D. L. Sackett, W. Losert, and R. Nossal, Spontaneous patterning of confined granular rods, Phys. Rev. Lett. **96**, 028002 (2006).

[8] J. Galanis, R. Nossal, W. Losert, and D. Harries, Nematic order in small systems: Measuring the elastic and wall-anchoring constants in vibrofluidized granular rods, Phys. Rev. Lett. **105**, 168001 (2010).

[9] L. Walsh and N. Menon, Ordering and dynamics of vibrated hard squares, J. Stat. Mech. (2016) 083302.

[10] L. F. Elizondo-Aguilera, A. Carrillo Ríos, G. M. Rodríguez-Liñán, F. López González, F. Donado, and F. Pacheco Vázquez, Structural and dynamical behavior of a vibrated granular system of hard-cubes, Physica A **632**, 129311 (2023).

[11] T. Müller, D. de las Heras, I. Rehberg, and K. Huang, Ordering in granular-rod monolayers driven far from thermodynamic equilibrium, Phys. Rev. E **91**, 062207 (2015).

[12] M. González-Pinto, F. Borondo, Y. Martínez-Ratón, and E. Velasco, Clustering in vibrated monolayers of granular rods, Soft Matter **13**, 2571 (2017).

[13] A. D. Armas, M. Maza-Cuello, Y. Martínez-Ratón, and E. Velasco, Domain walls in vertically vibrated monolayers of cylinders confined in annuli, Phys. Rev. Res. **2**, 033436 (2020).

[14] D. Dertli and T. Speck, In pursuit of the tetratic phase in hard rectangles, Phys. Rev. Res. **7**, L012034 (2025).

[15] M. V. Kurik and O. D. Lavrentovich, Defects in liquid crystals: Homotopy theory and experimental studies, Sov. Phys. Usp. **31**, 196 (1988).

[16] *Defects in Liquid Crystals: Computer Simulations, Theory and Experiments*, NATO Science Series II: Mathematics, Physics and Chemistry, edited by O. D. Lavrentovich, P. Pasini, C. Zannoni, and S. Žumer (Kluwer, 2001).

[17] S. Shankar, S. Ramaswamy, M. Cristina Marchetti, and M. J. Bowick, Defect unbinding in active nematics, Phys. Rev. Lett. **121**, 108002 (2018).

[18] D. J. G. Pearce, J. Nambisan, P. W. Ellis, A. Fernandez-Nieves, and L. Giomi, Orientational correlations in active and passive nematic defects, Phys. Rev. Lett. **127**, 197801 (2021).

[19] J. Nambisan, P. W. Ellis, and A. Fernandez-Nieves, The role of aspect ratio and activity on how active nematic defects distribute on toroidal surfaces, Mol. Phys. **122**, e2344623 (2024).

[20] A. de la Cotte, D. J. G. Pearce, J. Nambisan, and A. Fernandez-Nieves, Hidden order in active nematic defects, Proc. Natl. Acad. Sci. USA **122**, e2512147122 (2025).

[21] I. Musevicv, M. Skarabot, U. Tkalec, M. Ravnik, and S. Žumer, Two-dimensional nematic colloidal crystals self-assembled by topological defects, Science **313**, 954 (2006).

[22] M. Melle, S. Schlotthauer, M. G. Mazza, S. H. L. Klapp, and M. Schoen, Defect topologies in a nematic liquid crystal near a patchy colloid, J. Chem. Phys. **136**, 194703 (2012).

[23] U. Tu Lieu and N. Yoshinaga, Topological defects of dipole patchy particles on a spherical surface, Soft Matter **16**, 7667 (2020).

[24] M. González-Pinto, J. Renner, D. de las Heras, Y. Martínez-Ratón, and E. Velasco, Defects in vertically vibrated monolayers of cylinders, New J. Phys. **21**, 033002 (2019).

[25] M. Kleman and O. D. Lavrentovich, Topological point defects in nematic liquid crystals, Philos. Mag. **86**, 4117 (2006).

[26] M. J. Bowick and L. Giomi, Two-dimensional matter: Order, curvature and defects, Adv. Phys. **58**, 449 (2009).

[27] R. Wittmann, L. B. G. Cortes, H. Löwen, and D. G. A. L. Aarts, Particle-resolved topological defects of smectic colloidal liquid crystals in extreme confinement, Nat. Commun. **12**, 623 (2021).

[28] M. Robinson, C. Luo, P. E. Farrel, R. Erban, and A. Majumdar, From molecular to continuum modelling of bistable liquid crystal devices, Liq. Cryst. **44**, 2267 (2017).

[29] Y. Han, J. Yin, P. Zhang, A. Majumdar, and L. Zhang, Solution landscape of a reduced Landau-de Gennes model on a hexagon, Nonlinearity **34**, 2048 (2021).

[30] X. Yao, L. Zhang, and J. Z. Y. Chen, Defect patterns of two-dimensional nematic liquid crystals in confinement, Phys. Rev. E **105**, 044704 (2022).

[31] K. Zhao, R. Bruinsma, and T. G. Mason, Local chiral symmetry breaking in triatic liquid crystals, Nat. Commun. **3**, 801 (2012).

[32] A. P. Gantapara, W. Qi, and M. Dijkstra, A novel chiral phase of achiral hard triangles and an entropy-driven demixing of enantiomers, Soft Matter **11**, 8684 (2015).

[33] Y. Martínez-Ratón, A. Díaz-De Armas, and E. Velasco, Uniform phases in fluids of hard isosceles triangles: One-component fluid and binary mixtures, Phys. Rev. E **97**, 052703 (2018).

[34] J. W. Milnor, *Topology from the Differentiable Viewpoint* (Princeton University Press, 1997).

[35] I. W. Stewart, *The Static and Dynamic Continuum Theory of Liquid Crystals* (Taylor & Francis, London, 2004), Vol. 17.

[36] P. M. Chaikin and T. C. Lubensky, *Principles of Condensed Matter Physics* (Cambridge University Press, Cambridge, UK, 1998).

[37] J. Geng and J. V. Selinger, Theory and simulation of two-dimensional nematic and tetratic phases, Phys. Rev. E **80**, 011707 (2009).

[38] J. Vega, E. Velasco, and Y. Martínez-Ratón, Defects in vibrated monolayers of equilateral triangular prisms, https://astro-oled.es/datas/.